Geometry-Defined Response Time and Sensitivity for Microneedle-Based Amperometric Sensors

Marco Fratus, Jongcheon Lim, James K. Nolan, Emilee Madsen, Yumin Dai, Chi Hwan Lee, Jacqueline C. Linnes, *Member, IEEE*, Hyowon Lee, *Member, IEEE*, and Muhammad A. Alam, *Fellow, IEEE*

***Abstract*—Smart, ultrascaled, always-on wearable (and implantable) sensors are an exciting frontier of modern medicine. Among them, minimally invasive microneedles (MN) are an emerging technology platform for theragnostic applications. Compared to traditional continuous glucose measurement (CGM) devices, these MNs offer painless insertion and simple operation. These MN systems, however, rely on analyte diffusion from the interstitial fluid (ISF) to the sensing site, and thus, 1) introduce a substantial and intrinsic diffusion delay in sensor response, and 2) reduce the analyte concentration to which the sensor must respond. A diversity of experimental platforms has been proposed to improve performance, but their optimization relies on empirical iterative approaches. Here, we integrate the theory of transient flux balance and the biomimetic concepts from ion uptake by bacteria to derive a generalized physics-guided model for MN sensors. The framework suggests strategies to minimize response time and maximize extracted analyte concentration in terms of the geometric and physical properties of the system. Our results show that there exists an intrinsic tradeoff between response time and extracted analyte concentration. Our model, validated against numerical simulations and experiment data, offers a predictive design framework that would significantly reduce the optimization time for MN-based sensor platforms.**

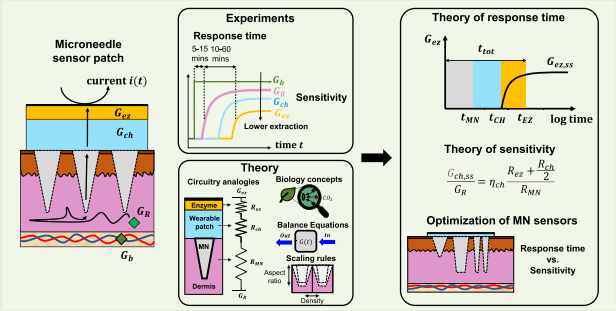

***Index Terms*— Amperometry, microneedle (MN) patch, modeling, response time, sensitivity, wearable and implantable (WI) sensors.**

I. Introduction

SMART healthcare, supported by ultrascaled, always-on digital electronics and wearable and implantable (WI) sensors, is an exciting and emerging frontier of modern medicine. Easier microfabrication, miniaturization, low-power, and -cost requirements have decentralized the testing site from traditional laboratories to "under or on skin" platforms [1], [2], [3], [4], [5]. Well-controlled laboratory-based measurements benefit from a well-defined availability of analyte supply, stable temperature, and closely monitored component degradation; therefore, their key focus is to develop high precision sensors with ultralow detection limit, fast response time, extended dynamic range, superior sensitivity, and selectivity [6], [7], [8], [9]. Correspondingly, significant efforts are devoted to defining the theoretical framework to explain, predict, and optimize the performance limits of laboratory-based sensors [10], [11], [12]. Many of the theoretical assumptions valid for laboratory measurements (e.g., analytes diffusing in a bulk solution) unfortunately do not hold for WI sensors; their analyte detection is complicated by uncontrolled transient processes (diffusion, enzymatic conversion, etc.,) across multiple domains (skin, interface, sensor patch, etc.) Therefore, it has been difficult to define response time, limits of detection,

Manuscript received 4 May 2023; accepted 12 May 2023. Date of publication 22 May 2023; date of current version 29 June 2023. This work was supported by Eli Lilly and Company. The work of Muhammad A. Alam was supported by the Jai N. Gupta Endowed Chair Fund. The associate editor coordinating the review of this article and approving it for publication was Dr. Chun Zhao. *(Corresponding author: Muhammad A. Alam.)*

Marco Fratus and Muhammad A. Alam are with the Elmore Family School of Electrical and Computer Engineering, Purdue University, West Lafayette, IN 47907 USA (e-mail: alam@purdue.edu).

Jongcheon Lim, James K. Nolan, Emilee Madsen, Jacqueline C. Linnes, and Hyowon Lee are with the Weldon School of Biomedical Engineering, Purdue University, West Lafayette, IN 47907 USA.

Yumin Dai is with the School of Materials Engineering, Purdue University, West Lafayette, IN 47907 USA.

Chi Hwan Lee is with the Weldon School of Biomedical Engineering, School of Mechanical Engineering, School of Materials Engineering, Purdue University, West Lafayette, IN 47907 USA.

This article has supplementary downloadable material available at https://doi.org/10.1109/JSEN.2023.3277425, provided by the authors.

Digital Object Identifier 10.1109/JSEN.2023.3277425

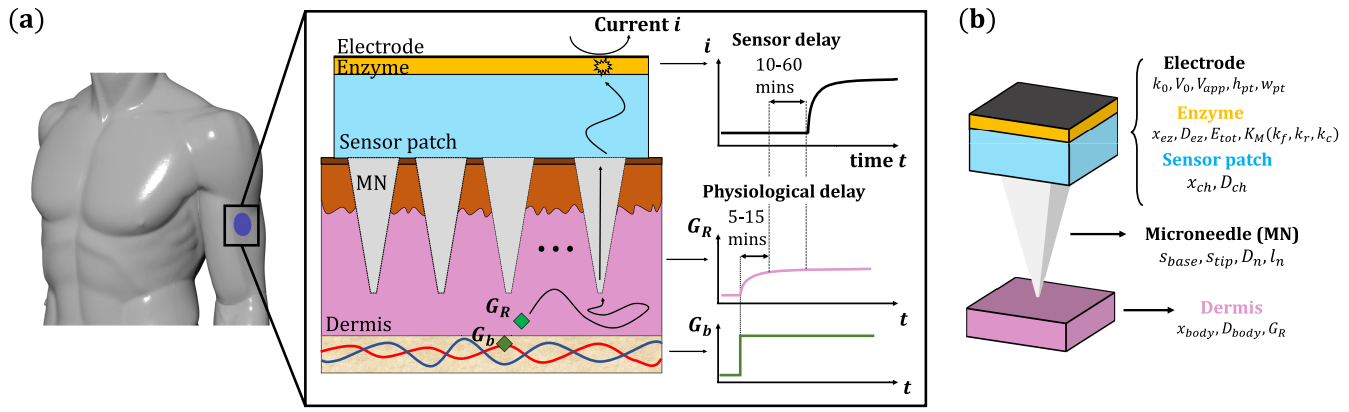

Fig. 1. (a) Illustration of a MN-based patch for ISF extraction. The sensor consists of MNs, sensor patch, and sensing site (enzyme-electrode). A lag time between variation of analyte concentration in the blood G_b and sensor response i delays the response. Diffusion between blood and dermis (first) and between dermis and sensing site (second) are the physiological and sensor-dependent sources of delay, respectively. (b) Unit cell of a generalized enzymatic electrochemical MN sensor with sensing site in an external wearable patch. The meaning of the parameters is described in S.I.

and/or sensitivity of this new class of sensors. The optimization is further complicated by WI-related considerations, such as biocompatibility [13], [14], [15], body-to-body variability [16], [17], [18], and limited energy supply [19], [20], [21]). Consequently, we must augment and reframe the theoretical framework for the design and optimization of WI sensors.

A microneedle (MN)-based patch is a minimally invasive analyte monitoring and drug delivery platform that allows continuous measurements over several weeks [22], [23]. The potential of combining disease diagnostics and drug delivery makes MN platforms suitable for closed-loop configurations, such as glycemic management and insulin therapy [24], [25], [26], [27], [28], [29]. Among the other geometric features (width, density, etc.) these MNs are substantially shorter (only a few hundred μm) compared to traditional millimeter-length hypodermic needles for continuous glucose measurement (CGM) devices, see Fig. 1(a). Thus, the MNs are minimally invasive and painless because there are fewer pain receptors in dermis compared to hypodermis [30], [31], [32], [33].

Among various modalities of MN-integrated sensors, electrochemical transduction combined with enzymatic conversion offers superior sensitivity and selectivity compared to colorimetric methods [18], [34], [35], [36], [37], [38], [39]. Once the interstitial fluid (ISF) accumulates in the patch, analyte molecules such as glucose G diffuse toward the enzyme-coated sensors. Here, they undergo the standard conversion (for example, in hydrogen peroxide, H_2O_2, and gluconic acid, $C_6H_{12}O_7$)

$$G + O_2 \rightleftarrows H_2O_2 + C_6H_{12}O_7. \tag{1}$$

The H_2O_2 molecules diffuse within the sensor patch until they reach the electrode interface for the redox reaction

$$H_2O_2 \rightleftarrows O_2 + n_{\text{el}} \tag{2}$$

where n_{el} is the number of generated electrons ($n_{\text{el}} = 2$). Unlike a hypodermic needle, where analytes are extracted by the vacuum created by the syringe, the analyte in passive MN sensors must reach the sensing surface by diffusion. The diffusion-delay introduces an intrinsic lag time between biofluid extraction and the sensor response, which could be problematic for many continuous in vivo applications. Specifically, Fig. 1(a) shows that ISF extraction experiences two sources of delays, namely 1) a physiological 5–15-min lag time between glucose variations in blood and corresponding changes in ISF ($G_b - G_R$ delay) [30], [40], [41], [42]; and 2) a sensor-dependent 10–60 min lag time between glucose variations in ISF and amperometric response in the wearable patch ($G_R - i$ delay) [13], [43], [44]. The MN-specific delay is significant; therefore, researchers have empirically explored the design-space by varying MN geometry (length, base, and tip apertures), MN composition (porous and swellable) [22], [26], [34], [36], ISF transport method (diffusion, capillary, and convection) [26], [34], [43] or sensing site (inside external patch, inside MN volume, on MN surface) [18], [35], [45], [46], [47]. Without a theory for MN sensors, however, the current design and optimization rely on time-consuming empirical iterative approaches [48]. Numerical simulations based on the finite element method have been used, but only to interpret specific experimental results [17], [49], [50]. Without a theoretical framework to rapidly explore the parameter space, it is difficult, if not impossible, to design, and optimize an MN sensor that would achieve the desired sensitivity with minimum response delay.

In this article, we develop a generalized physics-based model to analyze the geometry-dependent response delay and sensitivity observed in **hollow-type MN sensors** (ISF accessing the patch across the MN tip aperture). In Section II, we numerically simulate the time and position-dependent concentration of analyte molecules across the MN sensor. In Section III, we introduce the theoretical framework of overall transient response. In Section IV, we validate the model against numerical simulations and experiments. In Section V, we discuss guidelines and conclusions for sensor optimization.

II. Numerical Modeling

Fig. 1(a) shows a typical MN patch that accommodates hundreds of MNs per square centimeter. We will focus on

a unit cell defined by two rectangular domains (sensor patch and skin dermis) interconnected by a hollow parallelepiped with a square cross section (representing individual MNs), see Fig. 1(b). The enzymatic sensor is placed on the upper end of the sensor patch. We use the COMSOL Multiphysics finite-element software to simulate the impact of MN parameters on sensor response. We first define the fundamental physical processes within each domain, and guarantee flux continuity across the interfaces. The Fick's second law captures the analyte diffusion

$$\frac{\partial \rho}{\partial t} = \nabla \left(D_\rho \nabla \rho \right) \tag{3}$$

where ρ is the analyte concentration with diffusivity D_ρ in the corresponding domain (D_{body}, D_n, D_{ch} for skin, MN, and sensor patch, respectively). In the enzyme layer, the analyte dynamics consists of diffusion (with diffusivity D_{ez}) and enzymatic $G-\text{to}-H_2O_2$ conversion, assuming sufficient availability of O_2

$$\begin{aligned} E + G \underset{k_r}{\overset{k_f}{\rightleftharpoons}} \text{EG} &\xrightarrow{k_c} E + H_2O_2 \\ \frac{dG}{dt} &= -k_f E \cdot G + k_r \text{EG} \\ \frac{dE}{dt} &= -k_f E \cdot G + k_r \text{EG} + k_c \text{EG} \\ \frac{d\text{EG}}{dt} &= +k_f E \cdot G - k_r \text{EG} - k_c \text{EG} \\ \frac{dH_2O_2}{dt} &= +k_c \text{EG} \end{aligned} \tag{4}$$

where k_f, k_r, k_c are the rate constants for the forward, reverse, and catalytic steps of the conversion process with free enzyme concentration E. Mass conservation dictates $E_{\text{tot}} = E(t) + \text{EG}(t)$, where E_{tot} and $\text{EG}(t)$ are the total enzyme concentration and intermediate complex, respectively. Subsequently, the Butler–Volmer formalism describes the redox reaction on the electrode surface. By assuming an applied voltage higher than equilibrium potential, $V_{\text{app}} > V_0$, the H_2O_2 conversion dominates the reaction

$$i(t) \propto n_{\text{el}} k_0 \rho_{H_2O_2,s}(t) e^{\frac{(n_{\text{el}}-\alpha)\left(V_{\text{app}}-V_0\right)}{RT}} \tag{5}$$

where k_0 is the heterogenous rate constant, $\rho_{H_2O_2,s}(t)$ is the time-dependent hydrogen peroxide concentration at the electrode surface, T is the temperature, and α is the transfer coefficient. The simulation details are summarized in S.I.

The results of the COMSOL simulation are shown in Fig. 2. Fig. 2(a) plots G averaged within the enzyme volume, $(\overline{G}_{\text{ez}}(t))/G_R$, as a function of MN aperture s, MN length l_n, and MN diffusivity D. Here, G_R is the fixed glucose concentration in the dermis. The results confirm that the overall delay has several components. For the design corresponding to Fig. 2(a) (see S.I.), a minimum delay of approximately 15 minutes (10^3 s) is required for glucose to diffusion through the MN and the sensor patch before reaching the enzyme layer. Subsequent glucose accumulation and enzyme conversion produce an exponential response, reflected in the rapidly increasing amperometric current. Ultimately, the steady-state condition is reached in around 330 min ($2 \cdot 10^4$ s).

Although the diffusion–reaction kinetics are intuitive, it is not easy to quantify the role of individual MN parameters so to minimize the sensor response. Indeed, it is unclear why MN aperture and MN length so strongly impact the accumulated glucose concentration in the enzyme layer (micromolar in the patch versus millimolar in dermis), while the impact of their variation on the response time is essentially negligible, see Fig. 2(a) (left, center).

For additional insights at various stages of the time-response of $s = 25$ μm, Fig. 2(b) shows the 2-D snapshots of normalized G in the central plane of the MN sensor at $t_1 = 10^2$ s (left), $t_2 = 10^4$ s (center) and $t_3 = 10^5$ s (right). Similarly, Fig. 2(c) shows the normalized G (solid line) and H_2O_2 (dashed line) projections along the center cut at $t_1 = 10^2$ s (left), $t_2 = 10^4$ s (center) and $t_3 = 10^5$ s (right). Fig. 2(b) suggests the dynamics of glucose transport is complicated and the variation of glucose profile in the patch seems minimal, especially between $t = t_2$ and $t = t_3$ plots.

Fig. 2(c) offers significant insights regarding the spatial dynamics of the analyte molecules. In the dermis (pink background, 2500–3000 μm), G and H_2O_2 profiles show a negligible gradient; Instead, within the MN (gray background, 2000–2500 μm), sensor patch (light blue background, 30–2000 μm) and enzyme layer (orange background, 0–30 μm), the concentration profiles drop linearly. Specifically, the G profile ($t = t_2$ and $t = t_3$ plots) drops by 2–3 orders of magnitude in the MN compared to less than an order magnitude variation within the sensor patch. Within the enzyme layer, enzyme conversion, and electrode reaction are reflected in the substantial drop for G and H_2O_2 profiles. This slope, which is pinned at the electrode interface, is responsible for a constant amperometric current. Finally, the boundaries across the domains (dermis-MN, MN-sensor patch, MN-enzyme) show a nonlinear drop of analyte concentrations.

These observations anticipate the derivations of the analytical framework to be discussed in Section III, which will be pivotal in 1) decoupling the role of MN, sensor patch, and enzyme layer in MN response time and sensitivity, and thereby 2) justifying the concentration profiles shown in Fig. 2.

III. Transient Response of MN-Based Sensors

Here, we will show that the time-dependent response $\overline{G}_{\text{ez}}(t)$, calculated numerically and summarized in Fig. 2(a), can be analytically represented as

$$\frac{\overline{G}_{\text{ez}}(t)}{\overline{G}_{\text{ez,ss}}} = 1 + \left(\frac{\overline{G}_{\text{ez}}\left(t = t_{\text{MN}} + t_{\text{CH}}\right)}{\overline{G}_{\text{ez,ss}}} - 1 \right) e^{\frac{t-(t_{\text{MN}}+t_{\text{CH}})}{t_{\text{EZ}}}} \tag{6}$$

where $(t_{\text{MN}} + t_{\text{CH}})$ is the turn-on delay due to analyte transport through the MN and sensor patch. The exponential-like form has a time constant equal to t_{EZ} and steady-state concentration $\overline{G}_{\text{ez,ss}}$. Because the enzyme-related time (t_{EZ}) is the time constant of the exponential response, (6), t_{EZ} is defined as the time required by $\overline{G}_{\text{ez}}(t)$ to reach the 63% of its steady-state value. In the analysis below, we will derive analytical expressions for 1) the response time ($t_{\text{MN}}, t_{\text{CH}}, t_{\text{EZ}}$); 2) its steady-state concentration ($\overline{G}_{\text{ez,ss}}$); and 3) the averaged glucose concentration extracted in the patch ($\overline{G}_{\text{ch,ss}}$). The result

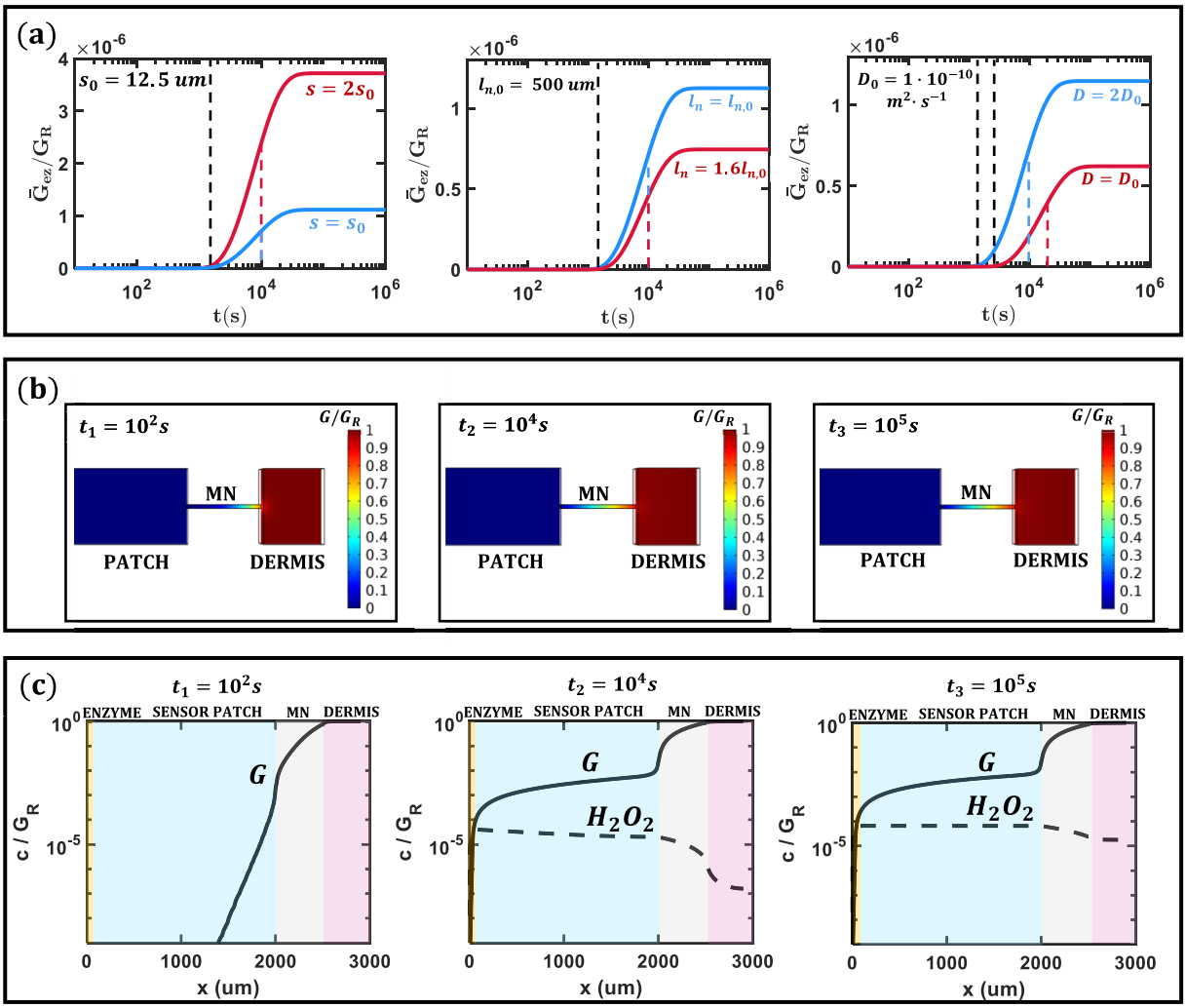

Fig. 2. COMSOL-based numerical simulations. (a) Impact of MN aperture $s_{base} = s_{tip} = s$ (left), MN length l_n (center), and MN diffusivity $D_{ch} = D_n = D$ (right) on normalized glucose concentration G averaged within the enzyme volume, $\bar{G}_{ez}(t)$. Related to the response for $s = 25$ μm (left, red line) in (a) and (b) are the 2-D snapshots of normalized G in the central plane at $t_1 = 10^2$ s (left), $t_2 = 10^4$ s (center) and $t_3 = 10^5$ s (right). The differences between $t = t_2$ and $t = t_3$ seem minimal. Related to the response for $s = 25$ μm (left, red line) in (a) and (c) are the normalized G and H_2O_2 projections along the center cut at $t_1 = 10^2$ s (left), $t_2 = 10^4$ s (center) and $t_3 = 10^5$ s (right). Here, enzyme layer (0–30 μm), sensor patch (30–2000 μm), MN (2000–2500 μm), and dermis (2500–3000 μm) are illustrated in orange, light blue, gray, and pink backgrounds, respectively. The electrode is at the origin (0 μm).

will capture the response time and sensitivity of MN systems as a function of the geometric and physical properties of the sensor system.

A. Theory of Response Time

Fig. 3 illustrates the MN sensor in terms of geometric and physical properties of the system, and its response (black line), at a fixed G_R (pink line). The total response time t_{tot} is the sum of individual contributions from MN, patch, enzyme layer

$$t_{tot} = t_{MN} + t_{CH} + t_{EZ} \tag{7}$$

where t_{MN} and t_{CH} are the time required by the analyte to diffuse across the MN and patch, respectively, and t_{EZ} is the effective time resulting from diffusion and reaction in the enzyme layer. Based on the linear profile drop shown in Fig. 2(c), we first approximate each domain as a diffusive resistor [s · m^{-3}] to be multiplied by the corresponding ISF volume to quantify the response time.

1) Transport Delay in the MN: The analyte extraction across MN tip and base is analogous to ion uptake by bacteria and gas flow across leaves stomata [51]. Similarly, the molecule transport along the MN length is analogous to the spreading resistance of a point contact [52]. Therefore, the resistance R_{MN} of the MN patch of size L^2 can be computed as a combination of N-parallel resistances (N MNs) as follows:

$$R_{MN} = \frac{1}{N}\left(R_{base} + R_n + R_{tip}\right). \tag{8}$$

The components of (8) are then expressed in terms of scaled variables $[l_n, r_T, r_B, r_i, x_{ch}]$ to generalize the framework for an arbitrary sensor design. Here, the variable r is the aspect ratio between MN length l_n and MN tip, base, and interspace, $r_T = (l_n/s_{tip})$, $r_B = (l_n/s_{base})$, $r_i = (l_n/s_i)$, with s_{tip} and s_{base} being half of tip and base MN aperture, respectively, s_i being the distance between two base sides, and x_{ch} being the patch

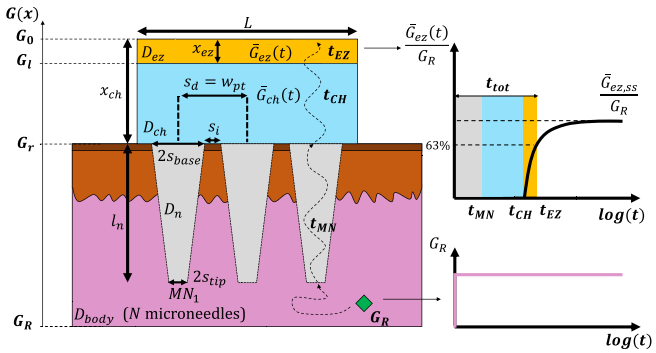

Fig. 3. Illustration of an MN sensor in terms of geometry- and composition-related parameters. (Right) Given a fixed glucose concentration in the dermis (G_R) (pink line), the delayed sensor response (black line) t_{tot} consists of individual contributions t_{MN}, t_{CH}, and t_{EZ}, to achieve the steady state condition $\overline{G}_{ez,ss}$. The ISF reaches the sensing site by accessing the MN across its tip aperture (gray domain) and diffusing across the patch (light blue domain) and enzyme layer (orange domain). G_r, G_l, G_0 are the glucose concentrations on bottom side (above MN base aperture) and top side of the patch (on enzyme-patch solution interface), and on the electrode surface, respectively.

thickness (see Fig. 3)

$$R_{\text{base}} \propto (D_{\text{ch}} s_{\text{base}})^{-1} = R_0 W_i w_{\text{base}} \tag{9}$$

$$R_n \propto l_n \left(D_n s_{\text{tip}}^2\right)^{-1} = R_0 W_i w_n \tag{10}$$

$$R_{\text{tip}} \propto \left(D_{\text{body}} s_{\text{tip}}\right)^{-1} = R_0 W_i w_{\text{tip}} \tag{11}$$

$$N = \left(\frac{L}{s_d}\right)^2 = \left(\frac{L}{s_i + 2s_{\text{base}}}\right)^2 = \frac{L^2 r_B^2}{4 l_n^2 W_i} \tag{12}$$

where

$$R_0 \equiv \frac{\pi}{4} \frac{l_n r_T}{D_{\text{body}} L^2 r_B^2} \tag{13a}$$

$$W_i \equiv 1 + \frac{r_B}{r_i} + \frac{r_B^2}{4 r_i^2} \tag{13b}$$

$$W_{\text{MN}} \equiv w_{\text{base}} + w_n + w_{\text{tip}} \tag{13c}$$

$$w_{\text{base}} \equiv \frac{D_{\text{body}}}{D_{\text{ch}}} \frac{r_B}{r_T} \tag{13d}$$

$$w_n \equiv \frac{4}{\pi} \frac{D_{\text{body}}}{\delta_n D_n} \frac{r_T}{r_T + 1} \left(r_T \left(\frac{r_B}{r_T}\right)^{\frac{2(r_T+1)}{r_T}} + 1 \right) \tag{13e}$$

$$w_{\text{tip}} \equiv 1. \tag{13f}$$

Equations (9)–(11) are diffusion resistances of base aperture, MN length, and tip aperture, respectively [51], [53]. Equation (13a) is the normalized resistance of the MN patch, (13b), (13c) are the correction factors W accounting for MN spacing (W_i, related to MN density) and MN sharpness (W_{MN}), respectively. The individual weights w are described in (13d)–(13f). The parameter δ_n in (13e) accounts for the dimensionality ($2 \le \delta_n \le 6$) of the analyte transport across the MN.

The transport time t_{MN} is the product of individual MN resistances, (9)–(11), and the corresponding effective volumes, V_{eff}

$$t_{\text{MN}} = R_{\text{base}} V_{\text{base,eff}} + R_n V_n + R_{\text{tip}} V_{\text{tip,eff}}. \tag{14}$$

For a MN shaped as a truncated pyramid, $V_n \equiv (4/3) l_n (s_{\text{base}}^2 + s_{\text{tip}}^2 + s_{\text{base}} s_{\text{tip}}) = (4/3) l_n^3 ((1/r_B^2) + (1/r_T^2) + 1/(r_B r_T))$, and $V_{\text{eff}}(l_n, r) = l_n((\zeta/l_n) + (\sigma/r))$ where $r = (l_n/s)$ is the scaled ratio, and ζ and σ are fitting parameters (see S.I.). The contributions from V_{eff} are important only for μm-sized MN patches. For typical MNs, $V_n \gg V_{\text{eff}}$, and $t_{\text{MN}} \approx R_n V_n$.

2) Transport Delay in the Sensor Patch: The concentration drop in the sensor patch during the initial transient is linear. Therefore, its diffusion time is the product between patch resistance R_{ch} and patch volume V_{ch}:

$$t_{\text{CH}} = R_{\text{ch}} V_{\text{ch}}. \tag{15}$$

For a parallelepiped patch of thickness x_{ch} and area w_{pt}^2

$$t_{\text{CH}} = \frac{\left(x_{\text{ch}} - x_{\text{base,eff}}\right)^2}{\delta_{\text{ch}} D_{\text{ch}}} \approx \frac{x_{\text{ch}}^2}{\delta_{\text{ch}} D_{\text{ch}}} \tag{16}$$

where $x_{\text{base,eff}} \propto s_{\text{base}}$ is the effective width of effective volume $V_{\text{base,eff}}$, and δ_{ch} accounts for the dimensionality ($2 \le \delta_{\text{ch}} \le 6$) of the analyte transport across the sensor patch.

3) Reaction Delay Due to Enzyme: The competition between analyte diffusion and enzyme reaction produces the exponential transient. Specifically, (4) governs the complex time-dependent interplay between the variables G, E, EG, and H_2O_2 through the enzyme conversion rates k_f, k_r, and k_c. An analytical solution for the time-dependent volume-averaged molecule profile is difficult. However, numerical simulations confirm that transport time across the sensor (rather than efficiency of enzyme conversion) dictates t_{EZ}. Fig. 4 shows the profile of G, E, EG, H_2O_2 molecules along the central cut of the enzyme layer at three subsequent times during the exponential rise. Unlike other molecules (G, H_2O_2, EG corresponding to solid, dashed, dotted lines), the free enzyme concentration (dash-dotted line) is essentially unchanged during the reaction transient. Because E is much higher than incoming G, the intermediate complex EG is limited to a very small amount; since $E + \text{EG} = E_{\text{tot}}$, we conclude $E \approx E_{\text{tot}}$ for the entire transient. In other words, the G supply limits the enzyme reaction

$$t_{\text{EZ}} = \gamma_{63} \left(R_{\text{base}} V_{\text{base,eff}} + R_n V_n + R_{\text{tip}} V_{\text{tip,eff}} + R_{\text{ch}} V_{\text{ch}}\right)$$
$$\approx \gamma_{63} R_{\text{ch}} V_{\text{ch}} = \gamma_{63} \frac{x_{\text{ch}}^2}{D_{\text{ch}}}. \tag{17}$$

Here, $\gamma_{63} \approx 1 - 2$ is a parameter calibrated to a single numerical simulation and kept unchanged for all designs.

B. Steady State Concentration

To derive an analytical form for $\overline{G}_{\text{ez}}(t)$, we integrate (4) and solve a flux balance for G in the enzyme layer

$$\frac{d\#_G}{dt} = N_A V_{\text{ez}} \frac{d\overline{G}_{\text{ez}}}{dt} = I_{G,\text{in}} - I_{G,\text{out}} - I_{\text{ez}} \tag{18a}$$

$$I_{G,\text{in}} - I_{G,\text{out}} \simeq N_A R_{\text{diff}}^{-1} \left(G_R - \overline{G}_{\text{ez}}\right) \tag{18b}$$

$$I_{\text{ez}} = N_A V_{\text{ez}} \frac{k_c E_{\text{tot}} \overline{G}_{\text{ez}}}{K_M + \overline{G}_{\text{ez}}} \simeq N_A V_{\text{ez}} \frac{k_c E_{\text{tot}}}{K_M} \overline{G}_{\text{ez}} \tag{18c}$$

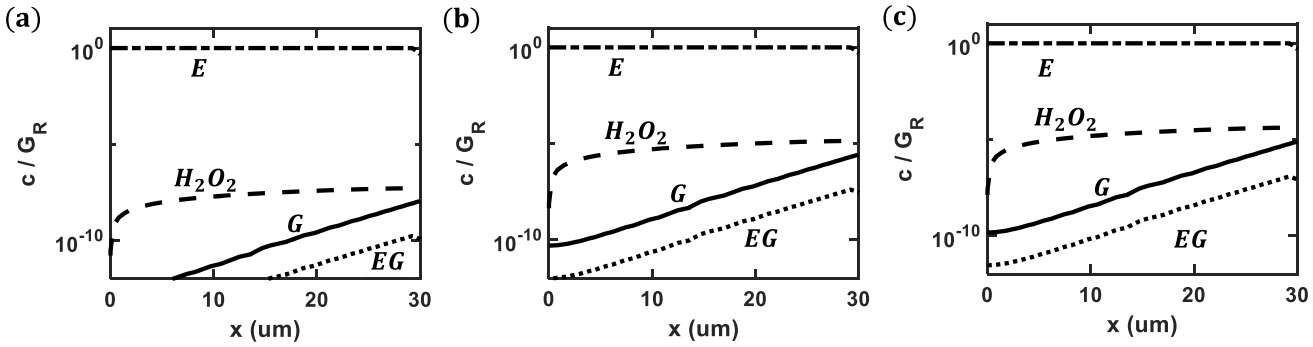

Fig. 4. COMSOL-based numerical simulations. Normalized molecule profiles (G, E, EG, H_2O_2) in the central cut of the enzyme layer for the sensor design discussed in Fig. 2(a), $s = 25\ \mu$m, at (a) $t_1 = 10^2$ s, (b) $t_2 = 10^4$ s, and (c) $t_3 = 10^5$ s. E, G, H_2O_2, EG concentration profiles are dash-dotted, solid, dashed, and dotted lines, respectively.

where $\#_G$ is the number of glucose molecules, $V_{ez} \equiv w_{pt}^2 x_{ez}$ is the enzyme volume (the unit cell has a square surface of side w_{pt} and thickness x_{ez}), N_A is the Avogadro number. Equation (18a) explains the G build-up in the enzyme is given by the balance of the incoming versus outgoing glucose fluxes [i.e., $I_{G,in} - I_{G,out}$, (18b)] and $G -$ to $- H_2O_2$ conversion flux [i.e., I_{ez}, (18c)]. Equation (18b) indicates that flux balance is dictated by the concentration differences and inversely proportional to the sensor resistance, $R_{diff} = R_{MN} + R_{ch}$. Equation (18c) is the Michaelis-Menten formalism, with K_M being the Michaelis-Menten constant. We assume 1) the enzymatic dynamics occurs at a faster time scale than the overall transport in the MN sensor and 2) $K_M \gg G_R \geq \overline{G}_{ez}$ for glucose concentrations in ISF [11]. The steady state solution of (18a) gives the following:

$$\frac{\overline{G}_{ez,ss}}{G_R} = \eta_{ez} \frac{\tau_{ez}}{\tau_{ez} + \tau_{diff}} \tag{19}$$

where $\eta_{ez} \approx 1$ is a parameter calibrated to a single numerical simulation and kept unchanged for all designs, $\tau_{ez} = R_{ez} V_{ez} = K_M/(k_c E_{tot})$, and $\tau_{diff} = R_{diff} V_{ez}$.

C. Extracted Analyte Concentration

Regardless of the transduction mechanism (colorimetric, electrochemical, etc.,) we define sensitivity and limit of detection as follows. Sensitivity is the relative change of the sensor response with respect to the input analyte concentration; the limit of detection is the minimum signal detectable by the instrumentation. For an MN sensor, we relate them to the analyte concentration accumulating in the patch, $\overline{G}_{ch,ss}$. $\overline{G}_{ch,ss}$ is a critical parameter to be assessed as the analyte concentration is scaled down across the MN by many orders of magnitude, as shown in Fig. 2(c). By degrading $\overline{G}_{ch,ss}$, the sensor may not satisfy the minimum signal level set by the noise limit, failing to register analyte fluctuations in the skin. Therefore, sensitivity and limit of detection must be defined in terms of geometric and physical properties of the system.

To derive $\overline{G}_{ch,ss}$, first we apply flux continuity among the domains in steady-state regime, and then average the contributions in the patch

$$\frac{G_R - G_r}{R_{MN}} = \frac{G_r - G_l}{R_{ch}} = \frac{G_l - G_0}{R_{ez}} \tag{20a}$$

$$\overline{G}_{ch,ss} \simeq \frac{G_r + G_l}{x_{ch}} \tag{20b}$$

where G_r, G_l, G_0 are the glucose concentrations on the bottom side (above MN base aperture) and top side of the patch (on enzyme-patch solution interface), and on the electrode surface, respectively (see Fig. 3). We combine (20a) and (20b) to get an expression for $\overline{G}_{ch,ss}$ in terms of MN sensor parameters

$$\frac{\overline{G}_{ch,ss}}{G_R} = \eta_{ch} \frac{R_{ez} + \frac{R_{ch}}{2}}{R_{MN}} \tag{21}$$

where $\eta_{ch} \approx 1$ is a parameter calibrated to a single numerical simulation and kept unchanged for all designs. Here, we assume 1) the electron transfer is not the limiting factor ($G_0 \approx 0$) and 2) $G_r \ll G_R$, see Fig. 2(c). For conventional MN sensors based on limited-analyte supply, $(R_{ch}/2) \geq R_{ez}$.

IV. Validation of the Results

A. Numerical Validation

We follow the sensor design described in Section II to validate the theoretical framework derived in Section III. The geometric and physical parameters are described in S.I.

Fig. 5(a1) and (a2) shows the excellent agreement between theoretical response, (6), and COMSOL numerical results for different MN geometric and physical parameters. Fig. 5(a1) confirms the linearity between $\overline{G}_{ez,ss}$ and G_R if $\overline{G}_{ez}(t) \ll K_M$ for a fixed MN geometry. Similarly, Fig. 5(a2) validates the impact of MN geometry, given a fixed G_R.

Fig. 5 also validates the theory of response time, Fig. 5(b1)–(e1), and sensitivity, Fig. 5(b2)–(e2) against COMSOL modeling as a function of geometric and physical parameters ($r_T = r_B = r$, l_n, D, x_{ch}).

The analytical model offers several insights. First, as shown in Fig. 5(b)–(e), the total response time [black line, (7)], ranges over many orders of magnitude (tens of minutes to tens of hours) depending on sensor geometry and physical properties. Diffusion time across the patch [t_{CH}, (16)], and enzyme-related delay [t_{EZ}, (17)] set the fundamental limit of the sensor.

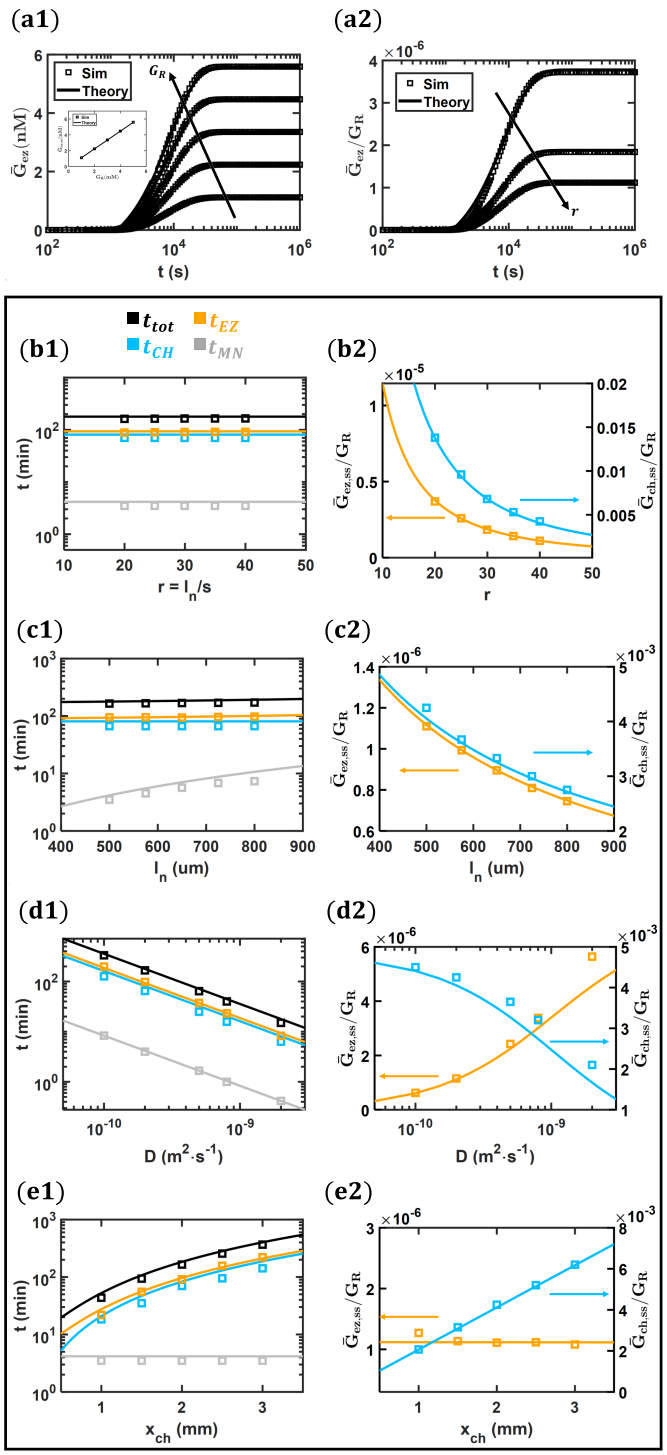

Fig. 5. Numerical validation. (a1) $\bar{G}_{ez}(t)$ for $G_R = 1, 2, 3, 4, 5$ mm. Inset is $\bar{G}_{ez}$ sensitivity plot. (a2) Normalized $\bar{G}_{ez}(t)$ for $r = (l_n/s) = 20, 30, 40$. Here, $\delta_n = 5$, $\delta_{ch} = 4$, $\gamma_{63} = 1.7$, $\eta_{ez} = 1.1$. Impact of (b) MN aspect ratio $r = (l_n/s)$, (c) MN length l_n, (d) MN and patch diffusivity D, (e) patch thickness x_{ch} on response time (t_{MN}, t_{CH}, t_{EZ}, t_{tot}) (b1)–(e1) and normalized glucose concentration $\bar{G}_{ez,ss}$, $\bar{G}_{ch,ss}$ (b2)–(e2). Here, $\delta_n = 5$, $\delta_{ch} = 4$, $\gamma_{63} = 1.1$, $\eta_{ez} = 1.1$, $\eta_{ch} = 4$. Solid line is the analytical theory, square symbols are COMSOL numerical results.

Finally, the design of MN does not affect the response time but plays a critical role in suppressing the availability of analyte concentration in the patch by several orders of magnitude [blue line, Fig. 5(b2)–(e2)].

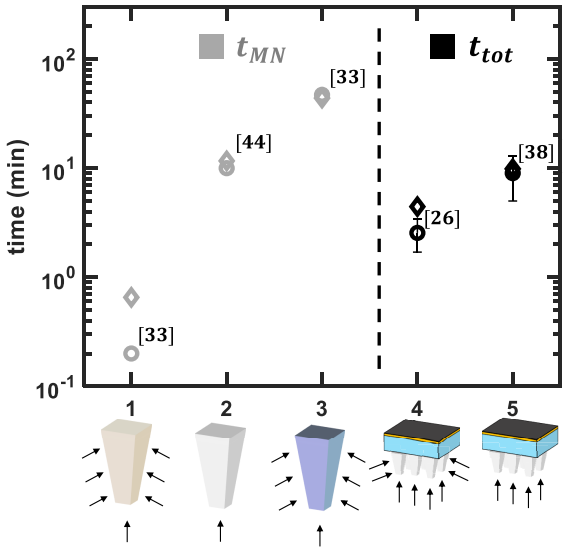

Fig. 6. Experimental validation. Theory (diamond symbol) versus experiments (circle symbol). t_{MN} and t_{tot} are gray and black symbols, respectively. MNs absorb analyte across tip aperture (MN 2) and lateral surface (MN 1 and 3 with corresponding diffusivity D_n). Sensors 4 and 5 absorb analyte across lateral surface and tip aperture, respectively. The fitting parameters are addressed in Table S2 in S.I. For MN 2, further details on fabrication and characterization are provided in S.I.

B. Experimental Validation

Fig. 6 shows the excellent agreement between the theory and experiments for a variety of MN sensors. Specifically, we apply (14) and (7) to assess t_{MN} (gray symbol) and t_{tot} (black symbol), respectively. Theoretical settings are discussed in S.I.

As expected, the theory predicts an experimentally observed delay of tens of minutes, excluding the physiological lag time. Although the model is derived for hollow-type MN sensors, the theory is easily generalized to other MN technologies with appropriate modification of the absorbing shape factor [54]. For example, to account for MNs absorbing ISF across their 3-D geometry (swellable or porous MNs), we introduce a shape factor ϵ_{abs} so that (14) becomes $t^*_{MN} = (t_{MN}/\epsilon_{abs})$ (See S.I.).

The small residual difference between theory and experiments may result from different sources. First, the effective dimension of MNs is not reported (MN tip, penetration length), and is estimated from the images included in the experimental papers. Second, an intrinsic variability affects material composition, with a corresponding impact on individual diffusivities. Third, the theory assumes passive transport operated by time-independent geometry of MNs (MN swelling is neglected). Despite these approximations, theoretical prediction anticipates/interprets the experimental results consistently and with high accuracy.

V. Discussion and Conclusion

MN technology has developed a broad diversity of platforms, which differ from each other for ISF extraction site (hollow versus swellable/porous), transport method (diffusion/capillary/convection forces), and sensing site (external sensor patch/on board/MN surface). The theoretical framework developed in this article suggests guidelines for design

and optimization of fast-response MN sensors. Overall, the response time t_{tot} ranges between tens of minutes to a few hours, offering significant room for improvement.

To minimize the response time, the contributions of (7) should be minimized and, if possible, eliminated. Among the approaches, optimization of sensor geometry with reduced patch thickness, MN length, and aspect ratios is the simplest to pursue. Thinner patches minimize diffusion time, but they also reduce the extracted analyte concentration, see Fig. 5(e1) and (e2). The diffusion time is also reduced if the sensing site is located close to the MN (on the MN surface or integrated within the MN volume). Also, high-diffusivity patches made of PBS [26] or MeHA [33] can substantially reduce the response time.

Once μm-sized patches are designed for a fast sensor response, MNs should be optimized. For conventional MNs, (14), (17), (19), (21) suggest that the role of the base aperture is negligible in the performance. Instead, length, tip aperture, and material composition should be carefully designed. The length should be minimized for a fast response (suppressed diffusion time R_nV_n) and increased extracted analyte concentration, see Fig. 5(c1) and (c2). Then, for a given resistance and extracted concentration, the tip aperture should be maximized, see Fig. 5(b1) and (b2). Finally, MN diffusivity must be optimized for the tradeoff between fast response time and extracted concentration, Fig. 5(d1) and (d2).

Although our theory was derived for a specific configuration (hollow MN/diffusive transport/external patch), the framework can be easily generalized for an arbitrary system by simple modifications. The model can be improved in several ways. First, WI devices suffer from time-dependent accumulation of biofouling material. This process degrades mechanical stability, and electrical performance, especially if the sensing site is on the MN surface. The model can be broadened to include biofouling deposition by adding an in-series resistive path $R_{BF}(t)$ to R_{MN}, (8). Second, although the model investigates electrical metrics (response time, sensitivity), an optimized design would include mechanical (MN insertion, buckling) and biocompatibility (inflammation) considerations. For example, while a shorter MN length would improve t_{tot}, the design choice may affect the depth of MN insertion in the skin. Similarly, a wider tip aperture, which would be beneficial for electrical performance, may cause more inflammation. More generally, its principles can be extended to investigate enzymatic sensors as part of modern devices. The electrical analogy (i.e., resistances associated with various segments of MN) used to model the ISF extraction is a generalized phenomenological approach to describe the operation of an arbitrary sensor technology; its applicability can be extended to study the deposition of functionalized layers, enzyme deactivation, sensor degradation [12]. Although not explicitly addressed, the role of capillary forces would be embedded in the theory of diffusion. The diffusivity coefficient of diffusion transport would be translated into an effective parameter capturing capillary transport.

To summarize, hollow-type MN sensors based on diffusive transport suffer from a slow design-dependent response. This is problematic as it limits the continuous monitoring of the analyte of interest. Compared to experimental and numerical efforts, a generalized analytical framework can predict the performance for an arbitrary sensor. Here, we developed a physics-guided model to describe MN response time and sensitivity in terms of geometric and physical properties of the system. Our model, validated against numerical simulations and experiments from a diversity of MN technologies, offers a predictive framework for design, and optimization of MN sensors. Its application can be broadened to investigate: 1) novel MN-based extraction mechanisms (porous, hydrogel); 2) challenges of biofouling deposition and, more generally; and 3) enzymatic sensors which combine kinetics of diffusion and reaction.

ACKNOWLEDGMENT

The authors gratefully acknowledge the reviewers for the thoughtful and constructive comments. They thank Michelle Pearson for coordinating the operations between Prof. Alam Group and Eli Lilly and Company.

Credit Authorship Contribution Statement: Marco Fratus: conceptualization, data curation, methodology, theoretical derivation, model fitting, validation, visualization, and writing. Jongcheon Lim, James K. Nolan, Emilee Madsen, and Yumin Dai: experiments and review manuscript. Chi Hwan Lee, Jacqueline C. Linnes, anad Hyowon Lee: supervision experiments and review manuscript. Muhammad A. Alam: supervision, review manuscript, and editing.

REFERENCES

[1] K. Mahato and J. Wang, "Electrochemical sensors: From the bench to the skin," *Sens. Actuators B, Chem.*, vol. 344, Oct. 2021, Art. no. 130178.

[2] H. Lee, Y. J. Hong, S. Baik, T. Hyeon, and D. Kim, "Enzyme-based glucose sensor: From invasive to wearable device," *Adv. Healthcare Mater.*, vol. 7, no. 8, Apr. 2018, Art. no. 1701150.

[3] C. Henry, "Getting under the skin: Implantable glucose sensors," *Anal. Chem.*, vol. 70, no. 17, pp. 594A–598A, Sep. 1998.

[4] Y. Xuan et al., "Fabrication and use of silicon hollow-needle arrays to achieve tissue nanotransfection in mouse tissue in vivo," *Nature Protocols*, vol. 16, no. 12, pp. 5707–5738, Dec. 2021.

[5] M. A. Alam, A. Saha, and M. Fratus, "Reliable sensing with unreliable sensors: Rethinking the theoretical foundation of field-deployed wearable/implantable/environmental sensors," *Innov. Emerg. Technol.*, vol. 9, Jan. 2022, Art. no. 2240003.

[6] T. N. H. Nguyen et al., "Printable nonenzymatic glucose biosensors using carbon nanotube-PtNP nanocomposites modified with AuRu for improved selectivity," *ACS Biomaterials Sci. Eng.*, vol. 6, no. 9, pp. 5315–5325, Sep. 2020.

[7] E. Danielson et al., "Non-enzymatic and highly sensitive lactose detection utilizing graphene field-effect transistors," *Biosensors Bioelectron.*, vol. 165, Oct. 2020, Art. no. 112419.

[8] S. Biswas, Q. Lan, Y. Xie, X. Sun, and Y. Wang, "Label-free electrochemical immunosensor for ultrasensitive detection of carbohydrate antigen 125 based on antibody-immobilized biocompatible MOF-808/CNT," *ACS Appl. Mater. Interfaces*, vol. 13, no. 2, pp. 3295–3302, Jan. 2021.

[9] R. M. Lubken, M. H. Bergkamp, A. M. de Jong, and M. W. J. Prins, "Sensing methodology for the rapid monitoring of biomolecules at low concentrations over long time spans," *ACS Sensors*, vol. 6, no. 12, pp. 4471–4481, Dec. 2021.

[10] X. Jin, T. S. Fisher, and M. A. Alam, "Generalized compact modeling of nanoparticle-based amperometric glucose biosensors," *IEEE Trans. Electron Devices*, vol. 63, no. 12, pp. 4924–4932, Dec. 2016.

[11] X. Jin and M. A. Alam, "Generalized modeling framework of metal oxide-based non-enzymatic glucose sensors: Concepts, methods, and challenges," *IEEE Trans. Biomed. Eng.*, vol. 67, no. 3, pp. 679–687, Mar. 2020.

[12] M. Fratus and M. A. Alam, "Universal scaling theory of electrochemical immunosensors: An analytical approach to define and compare performance metrics," *Appl. Phys. Lett.*, vol. 122, no. 5, Jan. 2023, Art. no. 054102.
[13] J. Li et al., "Interstitial fluid biomarkers' minimally invasive monitoring using microneedle sensor arrays," *Anal. Chem.*, vol. 94, no. 2, pp. 968–974, 2022.
[14] Y. Liu, Q. Yu, X. Luo, L. Yang, and Y. Cui, "Continuous monitoring of diabetes with an integrated microneedle biosensing device through 3D printing," *Microsystems Nanoengineering*, vol. 7, no. 1, p. 75, Sep. 2021.
[15] W.-C. Lee, N. G. Gurudatt, D.-S. Park, K. B. Kim, C. S. Choi, and Y.-B. Shim, "Microneedle array sensor for monitoring glucose in single cell using glucose oxidase-bonded polyterthiophene coated on AuZn oxide layer," *Sens. Actuators B, Chem.*, vol. 320, Oct. 2020, Art. no. 128416.
[16] A. Kadambi, "Achieving fairness in medical devices," *Science*, vol. 372, no. 6537, pp. 30–31, Apr. 2021.
[17] W. Shu, H. Heimark, N. Bertollo, D. J. Tobin, E. D. O'Cearbhaill, and A. N. Annaidh, "Insights into the mechanics of solid conical microneedle array insertion into skin using the finite element method," *Acta Biomaterialia*, vol. 135, pp. 403–413, Nov. 2021.
[18] M. Dervisevic et al., "Transdermal electrochemical monitoring of glucose via high-density silicon microneedle array patch," *Adv. Funct. Mater.*, vol. 32, no. 3, Jan. 2022, Art. no. 2009850.
[19] S. Yoo, J. Lee, H. Joo, S. Sunwoo, S. Kim, and D. Kim, "Wireless power transfer and telemetry for implantable bioelectronics," *Adv. Healthcare Mater.*, vol. 10, no. 17, Sep. 2021, Art. no. 2100614.
[20] K. K. Kim, J. Choi, and S. H. Ko, "Energy harvesting untethered soft electronic devices," *Adv. Healthcare Mater.*, vol. 10, no. 17, Sep. 2021, Art. no. 2002286.
[21] X. Jin, A. J. Bandodkar, M. Fratus, R. Asadpour, J. A. Rogers, and M. A. Alam, "Modeling, design guidelines, and detection limits of self-powered enzymatic biofuel cell-based sensors," *Biosensors Bioelectron.*, vol. 168, Nov. 2020, Art. no. 112493.
[22] J. G. Turner, L. R. White, P. Estrela, and H. S. Leese, "Hydrogel-forming microneedles: Current advancements and future trends," *Macromolecular Bioscience*, vol. 21, no. 2, Feb. 2021, Art. no. 2000307.
[23] H. Teymourian, F. Tehrani, K. Mahato, and J. Wang, "Lab under the skin: Microneedle based wearable devices," *Adv. Healthcare Mater.*, vol. 10, no. 17, Sep. 2021, Art. no. 2002255.
[24] B. A. Perkins, J. L. Sherr, and C. Mathieu, "Type 1 diabetes glycemic management: Insulin therapy, glucose monitoring, and automation," *Science*, vol. 373, no. 6554, pp. 522–527, Jul. 2021.
[25] L. Zhao et al., "Smart responsive microarray patches for transdermal drug delivery and biological monitoring," *Adv. Healthcare Mater.*, vol. 10, no. 20, Oct. 2021, Art. no. 2100996.
[26] X. Li et al., "A fully integrated closed-loop system based on mesoporous microneedles-iontophoresis for diabetes treatment," *Adv. Sci.*, vol. 8, no. 16, Aug. 2021, Art. no. 2100827.
[27] H. Park, A. Otte, and K. Park, "Evolution of drug delivery systems: From 1950 to 2020 and beyond," *J. Controlled Release*, vol. 342, pp. 53–65, Feb. 2022.
[28] R. Avila, C. Li, Y. Xue, J. A. Rogers, and Y. Huang, "Modeling programmable drug delivery in bioelectronics with electrochemical actuation," *Proc. Nat. Acad. Sci. USA*, vol. 118, no. 11, Mar. 2021, Art. no. e2026405118.
[29] J. Zhang, J. Xu, J. Lim, J. K. Nolan, H. Lee, and C. H. Lee, "Wearable glucose monitoring and implantable drug delivery systems for diabetes management," *Adv. Healthcare Mater.*, vol. 10, no. 17, Sep. 2021, Art. no. 2100194.
[30] F. Ribet, G. Stemme, and N. Roxhed, "Real-time intradermal continuous glucose monitoring using a minimally invasive microneedle-based system," *Biomed. Microdevices*, vol. 20, no. 4, Dec. 2018, Art. no. 2100194.
[31] J. D. Newman and A. P. F. Turner, "Home blood glucose biosensors: A commercial perspective," *Biosensors Bioelectron.*, vol. 20, no. 12, pp. 2435–2453, Jun. 2005.
[32] J. Xu, D. Xu, X. Xuan, and H. He, "Advances of microneedles in biomedical applications," *Molecules*, vol. 26, no. 19, p. 5912, Sep. 2021.
[33] P. Pradnya Samant and R. Mark Prausnitz, "Mechanisms of sampling interstitial fluid from skin using a microneedle patch," *Proc. Nat. Acad. Sci. USA*, vol. 115, no. 18, pp. 4583–4588, 2018.
[34] H. Lee, G. Bonfante, Y. Sasaki, N. Takama, T. Minami, and B. Kim, "Porous microneedles on a paper for screening test of prediabetes," *Med. DEVICES SENSORS*, vol. 3, no. 4, Aug. 2020, Art. no. e10109.
[35] J. W. Coffey, S. R. Corrie, and M. A. F. Kendall, "Rapid and selective sampling of IgG from skin in less than 1 min using a high surface area wearable immunoassay patch," *Biomaterials*, vol. 170, pp. 49–57, Jul. 2018.
[36] R. He et al., "A hydrogel microneedle patch for point-of-care testing based on skin interstitial fluid," *Adv. Healthcare Mater.*, vol. 9, no. 4, Feb. 2020, Art. no. 1901201.
[37] Y. Zeng et al., "Colloidal crystal microneedle patch for glucose monitoring," *Nano Today*, vol. 35, Dec. 2020, Art. no. 100984.
[38] A. Jina et al., "Design, development, and evaluation of a novel microneedle array-based continuous glucose monitor," *J. Diabetes Sci. Technol.*, vol. 8, no. 3, pp. 483–487, May 2014.
[39] K. Y. Goud et al., "Wearable electrochemical microneedle sensor for continuous monitoring of levodopa: Toward Parkinson management," *ACS Sensors*, vol. 4, no. 8, pp. 2196–2204, Aug. 2019.
[40] J. J. García-Guzmán, C. Pérez-Ràfols, M. Cuartero, and G. A. Crespo, "Microneedle based electrochemical (bio)sensing: Towards decentralized and continuous health status monitoring," *TrAC Trends Anal. Chem.*, vol. 135, Feb. 2021, Art. no. 116148.
[41] J. Madden, C. O'Mahony, M. Thompson, A. O'Riordan, and P. Galvin, "Biosensing in dermal interstitial fluid using microneedle based electrochemical devices," *Sens. Bio-Sensing Res.*, vol. 29, Aug. 2020, Art. no. 100348.
[42] E. Cengiz and W. V. Tamborlane, "A tale of two compartments: Interstitial versus blood glucose monitoring," *Diabetes Technol. Therapeutics*, vol. 11, no. S1, pp. 11–16, Jun. 2009.
[43] M. Zheng et al., "Osmosis-powered hydrogel microneedles for microliters of skin interstitial fluid extraction within minutes," *Adv. Healthcare Mater.*, vol. 9, no. 10, May 2020, Art. no. 1901683.
[44] D. H. Lee, E. A. Madsen, J. C. Linnes, and S. T. Wereley, "Temporally and spatially resolved micro-rheometry of a transient viscous polymer formation," *Meas. Sci. Technol.*, vol. 34, no. 3, Dec. 2022, Art. no. 035301, doi: 10.1088/1361-6501/aca993.
[45] J. Gao, W. Huang, Z. Chen, C. Yi, and L. Jiang, "Simultaneous detection of glucose, uric acid and cholesterol using flexible microneedle electrode array-based biosensor and multi-channel portable electrochemical analyzer," *Sens. Actuators B, Chem.*, vol. 287, pp. 102–110, May 2019.
[46] H. Teymourian et al., "Microneedle-based detection of ketone bodies along with glucose and lactate: Toward real-time continuous interstitial fluid monitoring of diabetic ketosis and ketoacidosis," *Anal. Chem.*, vol. 92, no. 2, pp. 2291–2300, Jan. 2020.
[47] P. R. Miller et al., "Hollow microneedle-based sensor for multiplexed transdermal electrochemical sensing," *J. Visualized Experiments*, no. 64, Jun. 2012, Art. no. e4067.
[48] P. R. Yadav, T. Han, O. Olatunji, S. K. Pattanayek, and D. B. Das, "Mathematical modelling, simulation and optimisation of microneedles for transdermal drug delivery: Trends and progress," *Pharmaceutics*, vol. 12, no. 8, p. 693, Jul. 2020.
[49] J. C. J. Wei et al., "Space- and time-resolved investigation on diffusion kinetics of human skin following macromolecule delivery by microneedle arrays," *Sci. Rep.*, vol. 8, no. 1, p. 17759, Dec. 2018.
[50] X. Q. Kong, P. Zhou, and C. W. Wu, "Numerical simulation of microneedles' insertion into skin," *Comput. Methods Biomechanics Biomed. Eng.*, vol. 14, no. 9, pp. 827–835, Sep. 2011.
[51] C. Howard Berg, *Random Walks in Biology*. Princeton, NJ, USA: Princeton Univ. Press, 2018.
[52] S. Karmalkar, P. V. Mohan, H. P. Nair, and R. Yeluri, "Compact models of spreading resistances for electrical/thermal design of devices and ICs," *IEEE Trans. Electron Devices*, vol. 54, no. 7, pp. 1734–1743, Jul. 2007.
[53] J. A. Greenwood, "Constriction resistance and the real area of contact," *Brit. J. Appl. Phys.*, vol. 17, no. 12, pp. 1621–1632, Dec. 1966.
[54] A. Bejan and A. D. Kraus, *Heat Transfer Handbook*. Hoboken, NJ, USA: Wiley, 2003.

Marco Fratus received the B.Sc. and M.Sc. degrees in biomedical and electrical engineering from the Politecnico di Milano, Milan, Italy, in 2014 and 2017, respectively, and the double M.Sc. degree in nanoelectronics from KTH, Stockholm, Sweden, in 2018. He is pursuing the Ph.D. degree with Purdue University, West Lafayette, IN, USA, focuses on modeling, design, optimization of wearable, and implantable electrochemical sensors.

As a Visiting Scholar at Columbia University, New York City, NY, USA, he investigated optoelectronic properties of graphene.

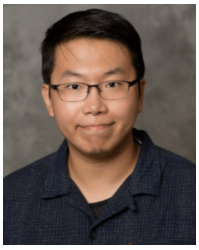

Jongcheon Lim received the B.S. degree in materials science and engineering from Yonsei University, Seoul, South Korea, in 2015, and the M.S. degree in bio and brain engineering from the Korea Advanced Institute of Science and Technology (KAIST), Daejeon, South Korea, in 2017. He is currently pursuing the Ph.D. degree in biomedical engineering from Purdue University, West Lafayette, IN, USA.

His research interests include implantable biosensors, microfabricated neural interface devices, and soft implantable materials.

James K. Nolan is pursuing the Ph.D. degree in biomedical engineering with Purdue University, West Lafayette, IN, USA.

His research interests include electrochemical biosensors for neurotransmitters and metabolic markers, applied to wearable devices, implantable devices, and microphysiometry.

Emilee Madsen is currently working as a Graduate Research Assistant with the Linnes Group, Purdue University, West Lafayette, IN, USA.

Yumin Dai is currently working as a Research Assistant with the Dr. Chi Hwan Lee's Research Group, Purdue University, West Lafayette, IN, USA. His research interests include fabrication, characterization, and application of wearable biosensors.

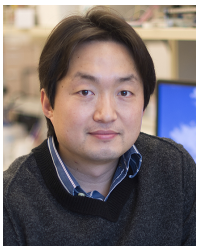

Chi Hwan Lee received the M.S. and Ph.D. degrees in mechanical engineering from Stanford University, Stanford, CA, USA, in 2009 and 2013, respectively.

He is the Lesli A. Geddes Associate Professor of Biomedical Engineering and an Associate Professor of Mechanical Engineering, and by Courtesy, of Materials Engineering at Purdue University, West Lafayette, IN, USA. Prior to joining Purdue University in 2015, he was a Postdoctoral Research Associate with the Department of Materials Science and Engineering, University of Illinois at Urbana-Champaign, Urbana, IL, USA, under the guidance of Prof. John A. Rogers. His scholarly efforts are dedicated to addressing unmet clinical needs using novel yet simple wearable devices with a clear path toward translation to produce measurable clinical and economic impacts.

Jacqueline C. Linnes (Member, IEEE) received the Ph.D. degree in bioengineering from the University of Washington, Seattle, WA, USA, in 2010.

She received the Graduate Certificate in global health at the University of Washington, followed by a postdoctoral training at Brigham and Women's Hospital, Boston, MA, USA, and Boston University, Boston. She is the Marta E. Gross Associate Professor with the Weldon School of Biomedical Engineering, Purdue University, West Lafayette, IN, USA, and also the Director of the College of Engineering Honors Program. Her inclusive interdisciplinary research laboratory develops point-of-care diagnostics, wearable devices, and global health technologies for underserved populations in the USA and abroad. Her work emphasizes the translation of fundamental microfluidics and biosensors into point-of-care diagnostics using human-centered design principles. Her experience in translational research includes co-founding and managing early-stage field-testing and user feedback for four startup companies.

Dr. Linnes is a Moore Inventor Fellow, a Kavli Frontiers of Science Fellow, an Executive Leadership in Academic Technology, and an Engineering and Science (ELATES) Fellow. She is a recipient of the NIH NIDA DP2 Avenir Award, the NIH NIBIB Trailblazer Award.

Hyowon Lee (Member, IEEE) received the B.A. degree in neuroscience from the Colorado College, Colorado Springs, CO, USA, in 2004, and the M.S. and Ph.D. degrees in biomedical engineering from UCLA, Los Angeles, CA, USA, in 2008 and 2011, respectively.

He started his professional career at St. Jude Medical, Saint Paul, MI, USA, as a Senior Engineer with the Implantable Electronic Systems Division, where he evaluated advanced technologies to facilitate manufacturing of next generation implantable medical devices. In 2014, he joined the Weldon School of Biomedical Engineering, Purdue University, West Lafayette, IN, USA.

Muhammad A. Alam (Fellow, IEEE) received the Ph.D. degree from Purdue University, West Lafayette, IN, USA, in 1995.

After a decade at Bell Laboratories, Murray Hill, NJ, USA, he returned to Purdue University in 2004, where he currently holds the Jai N. Gupta Professorship of Electrical Engineering. His research includes physics, performance limits, and novel concepts in biosensors, solar cells, and transistors. His most recent focus involves creating a theoretical foundation of wearable/implantable/environmental electrochemical sensors that would allow reliable sensing in unreliable environment.